16 December 2025

Electrochromic adaptive solar heater and sub-ambient passive daytime radiative cooler

Chenxi Sui[1], Yu Han[2], Qizhang Li[1], Xinyu Dou[2], Gangbin Yan[2], Jiadong Liu[1], Blake Harris[1], Jinlei Li[2], Alexander S. Filatov[1], Po-Chun Hsu[1]

1. University of Chicago
2. Stanford University

Abstract

Heating, ventilation, and air-conditioning (HVAC) systems are major contributors to global energy consumption, underscoring the urgent need for energy-efficient building envelope technologies. Synergistic solar and radiative electrochromism offers a promising solution by leveraging the sun and outer space as sustainable thermodynamic resources. In this study, we demonstrate a dual-mode electrochromic device that enables reversible, non-volatile switching between solar heating and sub-ambient radiative cooling, achieving an annual energy savings of 73.7 MBtu and CO2 emission savings of 4063 kgCO2 in specific U.S. climate zones. The device can achieve true sub-ambient passive daytime radiative cooling by 1 °C in the cooling mode and raise it by 33 °C above ambient in the heating mode during daytime operation, controlled by electrical voltage. The device employs electrodeposited lossy amorphous Cu-Bi nanoclusters on defect-activated monolayer graphene, yielding high optical contrast between cooling (solar absorptance # = 7.99%, thermal emittance # = 93.58%) and heating (# = 47.7%, # = 20.14%) modes, with outstanding long-term durability. This work paves the way for scalable, durable, and dynamic thermal regulation, advancing sustainable building technologies.

Keywords

Reversible Metal Electrodeposition, Radiative Cooling

Electrochromic adaptive solar heater and sub-ambient passive daytime radiative cooler

*Chenxi Sui[1,2], Yu Han[1], Qizhang Li[1], Xinyu Dou[3], Gangbin Yan[1], Jiadong Liu[1], Blake Harris[1], Jinlei Li[2], Alexander S. Filatov[4], Po-Chun Hsu[1]**

[1]Pritzker School of Molecular Engineering, University of Chicago, Chicago, IL, USA

[2]Department of Materials Science and Engineering, Stanford University, Stanford, CA, USA

[3]Department of Earth System Science, Stanford University, Stanford, CA, USA

[4]Department of Chemistry, University of Chicago, Chicago, IL, USA.

Abstract

Heating, ventilation, and air-conditioning (HVAC) systems are major contributors to global energy consumption, underscoring the urgent need for energy-efficient building envelope technologies. Synergistic solar and radiative electrochromism offers a promising solution by leveraging the sun and outer space as sustainable thermodynamic resources. In this study, we demonstrate a dual-mode electrochromic device that enables reversible, non-volatile switching between solar heating and sub-ambient radiative cooling, achieving an annual energy savings of 73.7 MBtu and CO_2 emission savings of 4063 kgCO_2 in specific U.S. climate zones. The device can achieve true sub-ambient passive daytime radiative cooling by 1 °C in the cooling mode and raise it by 33 °C above ambient in the heating mode during daytime operation, controlled by electrical voltage. The device employs electrodeposited lossy amorphous Cu-Bi nanoclusters on defect-activated monolayer graphene, yielding high optical contrast between cooling (solar absorptance α = 7.99%, thermal emittance ε = 93.58%) and heating (α = 47.7%, ε = 20.14%) modes, with outstanding long-term durability. This work paves the way for scalable, durable, and dynamic thermal regulation, advancing sustainable building technologies.

Main

Buildings consume 30% of global energy, with substantial heating and cooling loads required throughout the year. (*1-4*) Nearly 17% of the building energy consumption comes from heating, ventilation, and air-conditioning (HVAC) systems. This energy demand contributes to high operational costs and considerable greenhouse gas emissions, underscoring the urgent need for innovative solutions to improve energy efficiency. A promising approach to addressing this challenge is to leverage the sun (5,800 K) and the deep universe (3 K) for passive solar heating and radiative cooling, utilizing these inexhaustible thermodynamic heat/cold resources to regulate building temperatures with minimal energy input. (*3, 5-15*) However, due to the seasonal or even diurnal variation in weather conditions, the static and single-function approach of

radiative cooling or solar heating alone cannot address the dynamic thermal demands of buildings effectively. (*16-18*) In many places of the world with appreciable seasonal temperature variation, implementing single-function heating or cooling can incur even higher year-round energy consumption.(*16, 19*) The ideal net-zero-energy building should dynamically optimize its optical properties in response to changing weather conditions, providing adaptive thermal management that balances heating and cooling requirements in real-time. Ideally, in hot days, low solar absorptivity combined with high thermal emissivity facilitates radiative cooling. In contrast, in cold days, high solar absorptivity paired with low thermal emissivity enables efficient solar heating. (*20*)

Electrochromic devices are particularly well-suited for implementing dynamic and on-demand tuning of building optothermal conditions. (*21, 22*) They are compatible with existing building electricity systems, have low energy consumption, and allow on-demand switching between thermal states. Electrochromic devices , which dynamically regulate solar radiation through external voltage stimuli, offer significant potential for reducing building energy consumption and improving thermal comfort. However, traditional electrochromic technologies face key challenges in achieving simultaneous solar and mid-infrared optical tuning due to the narrow-band transmission of transparent electrodes.(*23-26*) As a result, their tunable range is primarily limited to the solar spectrum, often overlooking the benefits of mid-infrared modulation.(*27-29*) Similarly, mid-infrared electrochromic devices have been developed but largely missing the modulation of solar heat gain. (*30-34*) Although recent advancements have developed ultra-wideband transparent electrodes capable of addressing this challenge, low optical tuning contrast in the solar spectrum has hindered the ability to achieve sub-ambient radiative cooling, thus limiting energy-saving potential. (*20*) It is worth noting that only the true sub-ambient radiative cooling (that is, device temperature lower than the terrestrial air temperature that is measured without direct or indirect sunlight) can be considered thermodynamically advantageous compared with the trivial convective or conductive cooling.(*35*)

In this study, we address these challenges by developing an innovative electrochromic material and device system capable of reversible and non-volatile switching between solar heating and sub-ambient radiative cooling, catering to the dual thermal management needs of buildings. Through advanced device engineering, temporal modulation of electrochemical driving force, and the integration of a Cu-Bi amorphous nanocluster on defect-activated monolayer graphene, we achieve synergistic solar and mid-infrared optical tuning with a remarkable optical tuning contrast between radiative cooling (solar absorptance, $\alpha = 7.99\%$; thermal emittance, $\varepsilon = 93.58\%$) and solar heating ($\alpha = 47.7\%$; $\varepsilon = 20.14\%$) modes. Optical modeling and material characterization elucidate the underlying mechanisms of the high-performance optical tuning and electrodeposition process. Comprehensive building energy simulations reveal that this

electrochromic adaptive solar heater and radiative cooler can save up to 73.7 MBtu annually in specific U.S. climate zones. This breakthrough provides a scalable and effective route for enhancing energy savings and decarbonizing the building sector.

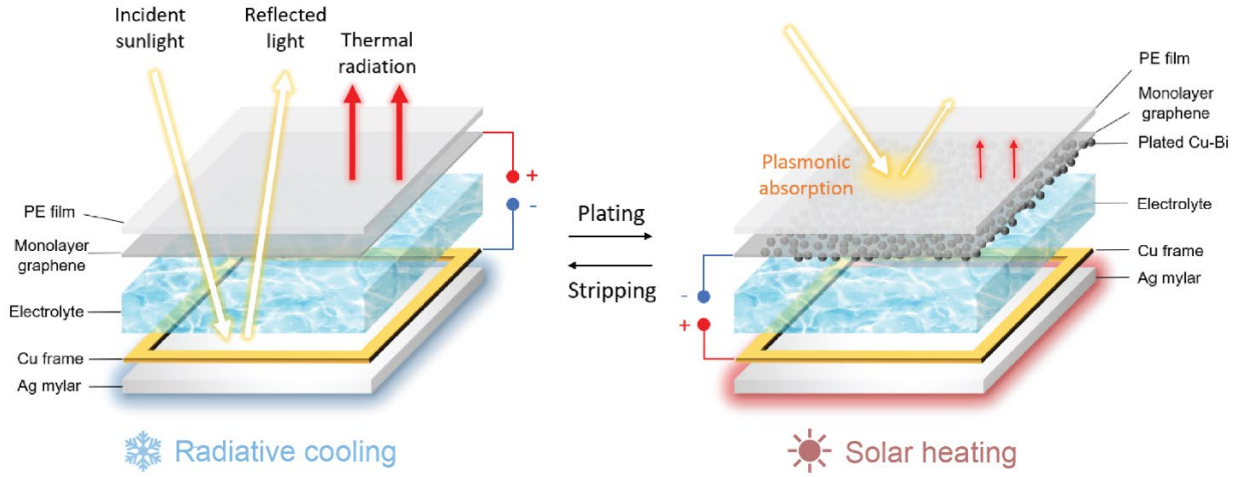

Figure 1. Schematics of the electrochromic adaptive solar heater and radiative cooler.

Pulse electrodeposition

Previous studies have demonstrated that ultra-wideband transparent electrodes, incorporating polyethylene (PE) film, a gold microgrid, and monolayer graphene, can achieve synergistic solar and mid-infrared tuning.(*20*) Because of the weak out-of-plane chemical interactions, graphene electrodes require a Pt nanoparticle seed layer to enable uniform and reversible metal electrodeposition. Without the Pt layer, metal deposition predominantly occurs around the metal grid, resulting in reduced optical tuning efficiency and reversibility. Unfortunately, this Pt nanoparticles seed layer also strongly absorbs sunlight via localized surface plasmon resonance, preventing the device from achieving a sub-ambient radiative cooling state.(*20*)

While it is tempting to eliminate both the gold microgrid and the nano-Pt layer to enhance the device's electrochemical tuning efficiency and optical performance, the removal of these conductive components introduces a critical issue: the intrinsic electrical conductivity of monolayer graphene alone is insufficient compared to the modified transparent electrode.(*20, 36*) This results in a significant ohmic potential drop across the graphene plane, impairing the uniformity of electrodeposition and reducing optical tuning efficiency. To overcome this limitation, we employed pulse electrodeposition, a technique used in metal plating to control deposition morphology.(*37-39*) The large transient voltage overcomes the nucleation threshold overpotential for the entire graphene electrode, creating densely distributed metal nanoparticles that not only increase the electrical conductance but also catalyze the subsequent growth. By leveraging this approach, we improved the uniformity and

density of metal deposition, effectively compensating for the absence of the conductive grid and Pt modification.

Fig. 2A illustrates the voltage profile of the pulse electrodeposition process of Cu-Bi alloy, which comprises three distinct steps. Step I involves a short-duration, high-voltage process designed to uniformly deposit a thin layer of Cu-Bi nanoparticles across the graphene surface. This phase corresponds to the nucleation step (Fig. 2B). Applying a higher deposition voltage (-3 V) overcomes the potential drop caused by monolayer graphene, enabling uniform metal nanoparticle deposition with consistent morphology across both the center and edge of the electrode (Fig. 2C and 2D). In contrast, under conventional deposition voltage (-1 V), most of the metal accumulates near the electrode's edges due to the ohmic drop (Fig. 2E and 2F). In addition to microscale characterization, macroscale optical imaging further validates this phenomenon. (Supplementary Fig. 1) Importantly, the duration of high voltage is short enough to prevent noticeable hydrogen evolution. The resulting uniformly distributed metal nanoparticles improve electrodeposition uniformity during subsequent steps. In essence, this step works as an in-situ and redox-reversible modification of graphene with metal nanoparticles to enhance its electrochemical properties, successfully circumventing the undesirable solar absorption from the nano-Pt modification. Step II changes the potential to -1 V, allowing the deposited metal particles to grow larger and denser (Fig. 2B). As the electrodeposited charge density increases, the nanoparticles coalesce into a more continuous layer (Fig. 2G), and the voltage is removed after the optical property stops changing. Using Cu^{2+}/Cu^{0} as the counter electrode ensures the electrodeposition is non-volatile, allowing the Cu-Bi nanoparticles to remain in place, which enables strong solar heating without requiring additional electrical energy and guarantees high tuning efficiency of the system.

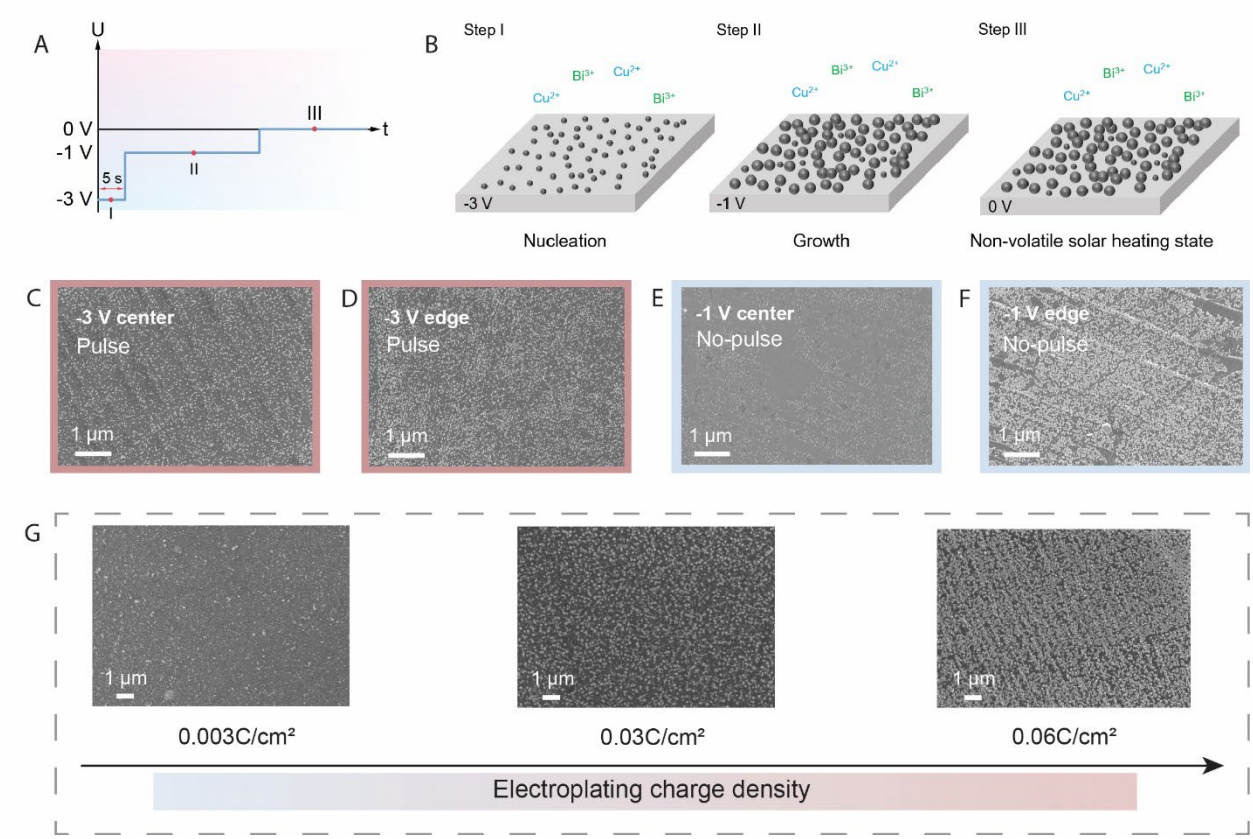

Figure 2. Pulse electrodeposition process. (A) Voltage profile of the pulse electrodeposition process. (B) Schematic representation of material growth during each step. (C-F) Scanning electron microscopy (SEM) images showing metal deposition at different locations on the graphene electrode under varying voltages. C and D correspond to pulse deposition, and E and F correspond to no-pulse deposition. (G) SEM images illustrating metal deposition at different charge densities.

Absorption enhancement by amorphous metal

During the growth stage of electrodeposition, we observed that the solar absorptivity continues to increase until it saturates, an intriguing phenomenon distinct from that of Cu. In Cu electrodeposition, the solar reflectivity tends to drop significantly when Cu nanoparticles begin to coalesce. (*40*) This is because the merged Cu nanoparticles become larger and larger compared with the skin depth, which exhibits the mirror behavior rather than localized surface plasmon resonance. On the other hand, the thermal emissivity decreases monotonically as the charge density increases. So, what makes Cu-Bi so special? We speculate that certain microstructural reasons prohibit coalescence from the optical material science standpoint. Further X-ray diffraction

characterization indicates that Cu-Bi has unusually low crystallinity. (Supplementary Fig. 2) Compared to crystalline metals, amorphous metals hold greater potential for sunlight absorption due to their lower intrinsic electrical conductivity.(*41*). Morphologically, clusters of small nanoparticles can capture more light compared to a single nanoparticle of similar size. It is therefore hypothesized that the immiscibility of Cu and Bi can hinder crystallization and promote the formation of clusters of small nanoparticles (Fig. 3A). (*42*) By utilizing Cu-Bi electrolyte, it becomes possible to create amorphous metal films that exhibit both low emissivity and high solar absorptivity.

To validate this, we measured the solar absorptivity of devices fabricated with Cu and Cu-Bi electrolytes (Fig. 3B). The results show that the Cu-Bi device achieves significantly higher solar absorptivity. For Cu, only the interband transition for wavelengths below 600 nm contributes to the absorption. The morphology and elemental distribution of the deposited metal nanoparticles were characterized using cross-sectional scanning transmission electron microscopy (STEM). High-angle annular dark-field (HAADF) imaging revealed a metal film composed of nanoclusters approximately 50 nm in diameter (Fig. 3C). Zooming into a single cluster (Fig, 3D–3F), energy-dispersive X-ray spectroscopy (EDS) mapping confirmed that Cu and Bi are evenly distributed with a Cu:Bi atomic ratio of 3:1. The reduction potentials of Cu and Bi in the same electrolyte environment are similar (theoretical values are both 0.281 V in our electrolyte) and exceed the applied voltage (-1 V), allowing the simultaneous deposition of both metals. (Supplementary Fig. 3) Since Cu and Bi are immiscible(*43*), this single cluster is essentially composed of numerous smaller Cu and Bi nanoparticles. Furthermore, the selected area electron diffraction (SAED) pattern (Fig. 3G), which lacks any noticeable crystalline structure, confirms the amorphous nature of the deposited metal. While amorphous/glassy metals are traditionally synthesized through rapid quenching under stringent thermal processing conditions, we demonstrate that the electrodeposition method can also produce amorphous metal films at room temperature, an outcome of rapid solidification from the ionic form.

To further elucidate the enhanced solar heating performance, we used finite element modeling (COMSOL Multiphysics) to simulate the solar absorptivity of Cu and Bi with different morphologies. The refractive indices of Cu and Bi are built into the software library. Two models were analyzed: a single large particle and a cluster of smaller particles with equivalent overall size (Fig. 3H, inset). The simulation results show that nanocluster morphology significantly enhances solar absorptivity for both Cu and Bi compared to single Cu particles. Electric field distribution simulations indicate that the clusters exhibit stronger resonances, further enhancing their light-harvesting capability (Fig. 3J). This highlights the critical role of morphology in improving the optical performance of the Cu-Bi nanoclusters. While previous works have utilized Cu–Bi for color-neutral electrochromics, the optical mechanism has not been fully explained. (*28,*

44) Here, our simulation offers a clearer insight into how nanocluster morphology enhances light absorption, thereby complementing and advancing this understanding.

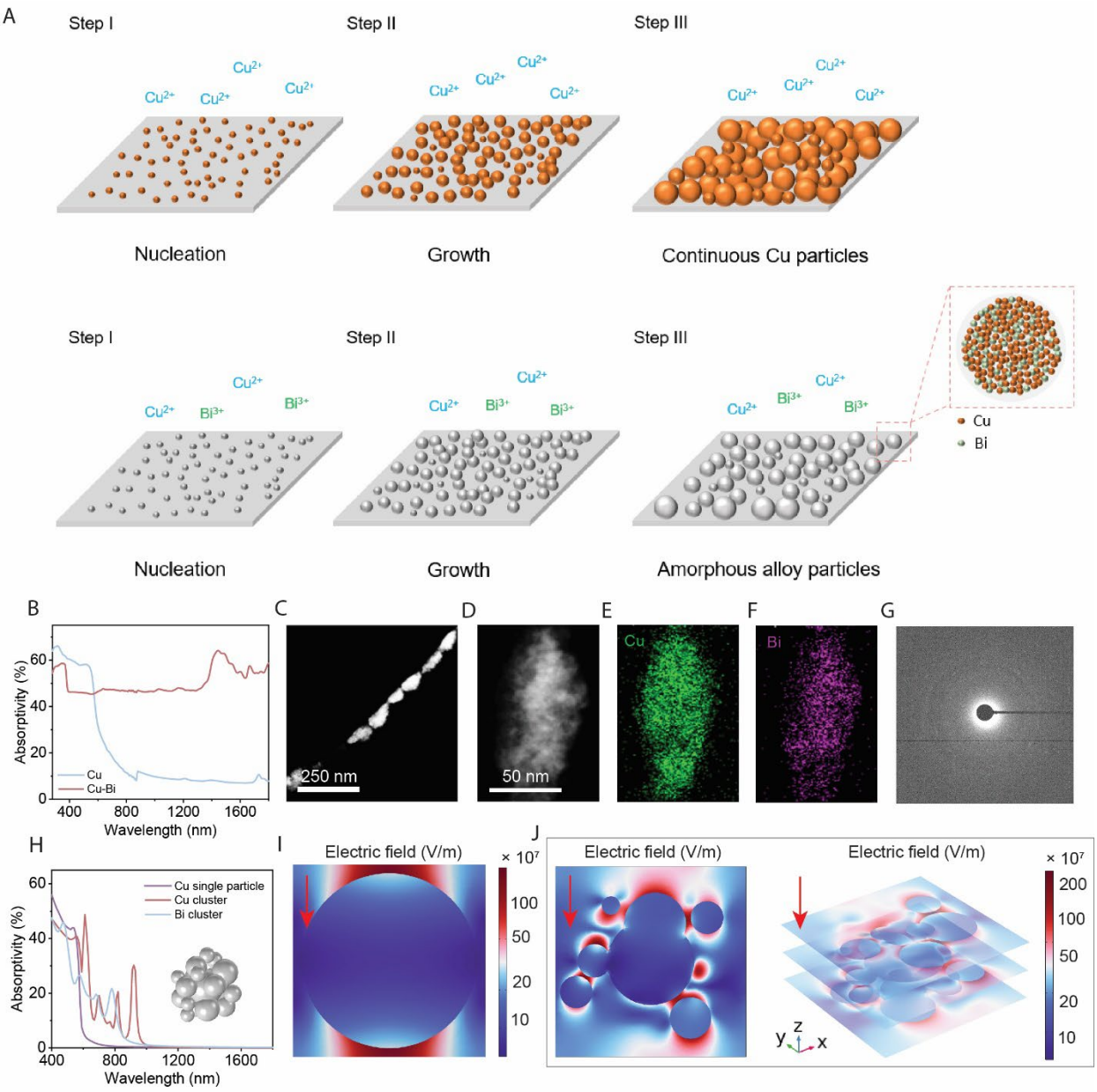

Figure 3. Characterization and optical properties of amorphous Cu-Bi nanoparticles. (A) Schematic illustration of the electrodeposition process for amorphous Cu-Bi nanoparticles. (B) Comparison of solar absorptivity between electrochromic devices using Cu and Cu-Bi electrolytes. (C, D) Cross-sectional STEM images of the deposited Cu-Bi nanoparticles. (E-G) EDS mapping and electron diffraction patterns of the Cu-Bi nanoparticles. (H) Simulated solar absorptivity of various materials with different

morphologies, highlighting the optical advantages of the Cu-Bi nanocluster. (I, J) Simulated electric field distribution around a single Bi nanoparticle and a cluster of Bi nanoparticles at λ = 550 nm. Specifically, the first image in (J) shows the cross-section on the xy-plane at the middle position along the z-axis, while the second image presents a series of cross-sectional views on various xy-planes. The red arrow specifies the direction of electromagnetic wave propagation.

Defect-activated graphene for enhanced electrodeposition

Pristine monolayer graphene typically exhibits limited electrochemical active sites for the electrodeposited metals, resulting in sparse and non-uniform electrodeposition. While the pulsed electrodeposition approach resolves the non-uniformity caused by the ohmic loss, graphene's out-of-plane chemical inertness can cause non-uniformity at the micron scale. To address this, modifying the graphene to introduce additional nucleation sites is crucial for achieving dense and uniform metal deposition. Our findings indicate that the hot-press transfer process of graphene onto PE film and the oxidative etching of Cu foil inherently introduces O-C=O defects, as confirmed by X-ray photoelectron spectroscopy (XPS) analysis (Fig. 4A and 4B). These functional groups have strong positive correlation with the uniformity and density of metal deposition compared to pristine graphene (Fig. 4C and 4D).

We attribute this enhancement to the role of O–C=O functional groups as localized nucleation sites. These defect sites disrupt the otherwise chemically inert sp² carbon network, creating localized regions with higher surface energy and charge localization, which in turn can attract metal cations and anchor the electrodeposited metal, promoting more uniform and continuous growth of the metal layer across the graphene surface.

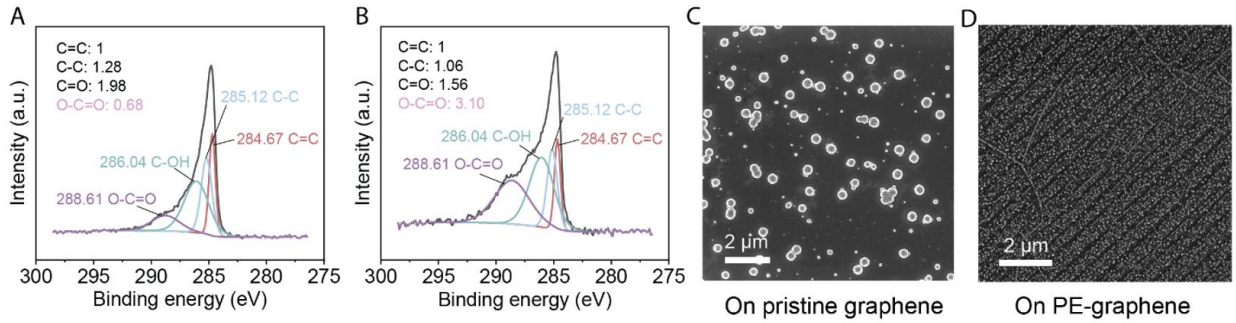

Figure 4. Graphene modification for improving electrodeposition. (A, B) C K-edge XPS analysis for pristine and transferred graphene. (C, D) SEM images of electrodeposited Cu-Bi on pristine and transferred graphene.

Device optical performance

With the enhanced electrodeposition uniformity achieved by pulsed electrodeposition and defect activation (without the adverse effects of Pt nanoparticles) and the improved solar absorption properties of amorphous Cu-Bi nanoclusters, the next task is to design the electrochromic device capable of achieving both sub-ambient radiative cooling and solar heating. In particular, sub-ambient radiative cooling requires substantial solar reflectance, so any undesired absorption should be further minimized by device engineering. First of all, we optimized the electrolyte thickness to minimize the electrolyte optical path while ensuring enough ion species areal density for electrodeposition. (Supplementary Fig. 4) To accomplish sub-ambient radiative cooling, we further enhanced the device's solar reflectivity by applying a hot-pressed 80 μm PE film as a top cover filter (Supplementary Fig. 5). Fig. 5A illustrates the full spectrum of the device in both heating and cooling states. In the heating state, the device achieves a solar absorptivity of 47.70% and a thermal emissivity of 20.14%. Conversely, in the cooling state, the device exhibits a solar absorptivity of 7.99% and a thermal emissivity of 93.58%. The device behaves as a high-emissivity solar mirror in the radiative cooling mode and a low-emissivity solar absorber in the solar heating mode. (Supplementary Fig. 6) Durability tests confirm that the solar absorptivity and thermal emissivity can be reversibly tuned over 1,000 cycles (Fig. 5B). Degradations in the tuning contrast of solar absorptivity and thermal emissivity were observed, which can likely be attributed to side reactions such as hydrogen evolution reaction. This phenomenon is indicated by an increase in the pH of the electrolyte (Supplementary Fig. 7), suggesting proton consumption during cycling. Protons play a crucial role in facilitating efficient electrodeposition and stripping processes, and their depletion may adversely affect device performance. (*28, 40*) Future electrolyte designs can help mitigate this issue. For instance, water-in-salt electrolytes can suppress proton-related side reactions by reducing free water activity (*45*) (*46*). Ionic-liquid systems eliminate hydrogen evolution and improve electrode reversibility (*47*). Alternatively, using chelating agents or operating in mildly alkaline complexing electrolytes can stabilize metal ions and suppress proton reduction (*48*). Furthermore, thanks to the non-volatile nature of the electrodeposition process, the device's heating and cooling states can be dynamically tuned and then maintained without any electricity input, as shown in Fig. 5C. Given its exceptional optical tuning capability, we conducted an outdoor test to demonstrate the temperature management performance of the electrochromic device (Figs. 5D–F). The test took place on May 14, 2025, on the rooftop of the Electrical Engineering Building at Stanford University. The results show that, under direct sunlight, the device in cooling mode was able to reduce the temperature to approximately 1 °C below ambient, while in

heating mode, it increased the temperature by an average of about 33 °C above ambient (Figs. 5G and 5H).

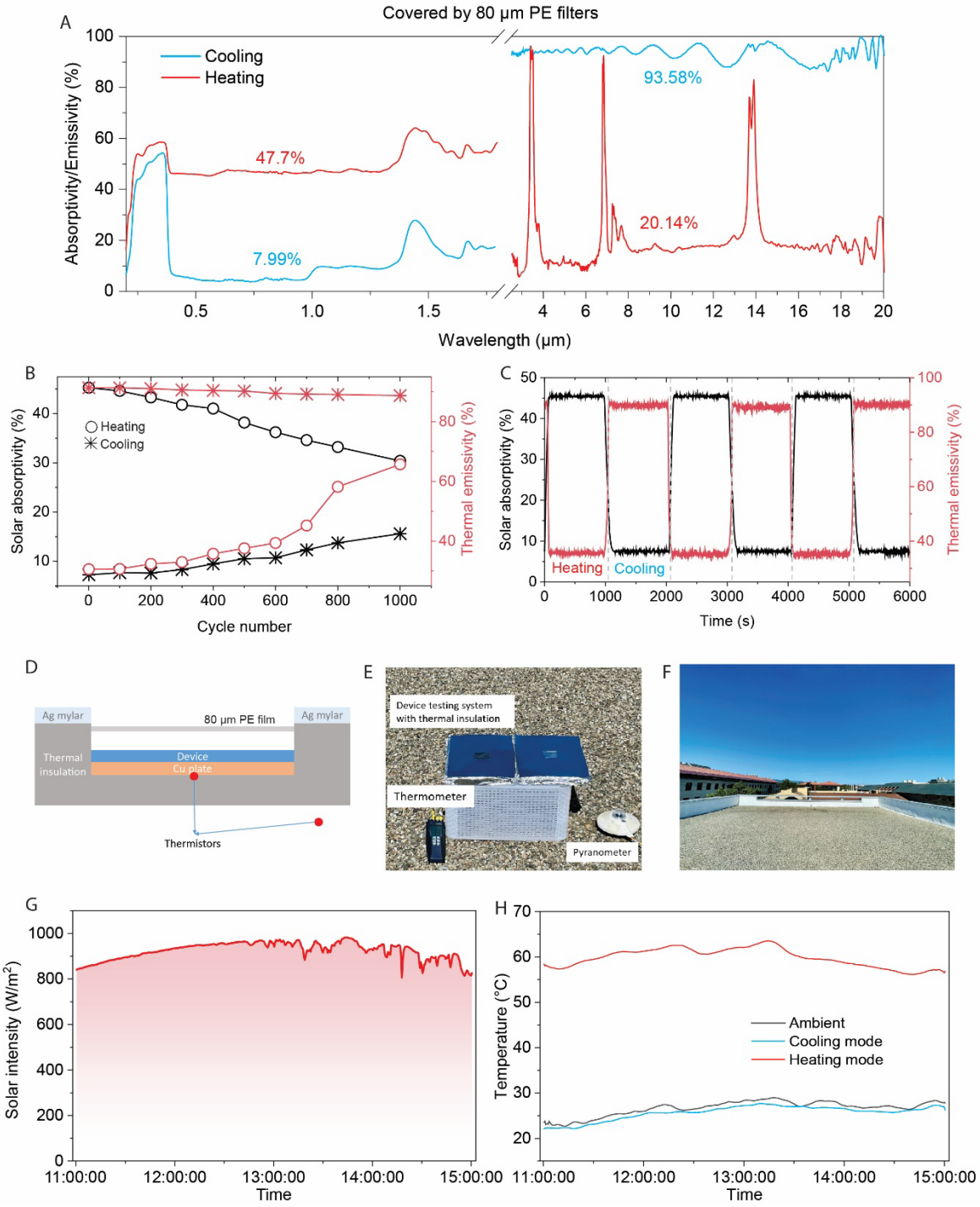

Figure 5. Synergistic electrochemical tuning of solar and mid-infrared optical properties. (A) UV-Vis and Fourier Transform Infrared

Spectroscopy (FTIR) measurements illustrating the optical properties of the device in both heating and cooling states. (B) Durability test demonstrating the electrochemical tuning stability over 1000 cycles. (C) Non-volatile and dynamic tuning of solar absorptivity and thermal emissivity. After the device reaches the heating or cooling state, the applied voltage is turned off, maintaining the state without further electrical input. (D, E) Schematics and photographs of the outdoor test setup. (F) Photograph of the outdoor test location on the rooftop of the Electrical Engineering Building at Stanford University. (G, H) Measured solar intensity and device temperatures under cooling and heating modes.

Building energy and CO_2 emission saving capability

The exceptional performance of the electrochromic adaptive solar heater and radiative cooler demonstrates its significant potential for reducing HVAC energy consumption in buildings. When installed on rooftops, the device facilitates heat radiation into deep space during hot seasons and absorbs sunlight for heating in cold seasons (Fig. 6A). To assess its energy-saving potential, *EnergyPlus* simulations were conducted for a building equipped with an electrochromic device. Fig. 6B illustrates the HVAC loads over the course of a year for a mid-rise apartment (Supplementary Fig. 8) in Chicago, highlighting the high and consistent energy demand throughout the year. Following the installation of the electrochromic device, an average energy savings of 73.69 MBtu annually was observed across the U.S. regions. Due to the device's effective sub-ambient radiative cooling performance, more significant energy savings are realized in warmer climates compared to colder regions (Fig. 6C and 6D). This underscores the need for further advancements in materials and electrochemical optimization to enhance the solar heating efficiency of electrodeposited metals. To highlight the environmental benefits of this electrochromic device, we further calculated the annual CO_2 emission savings across the U.S. (Fig. 6E and 6F). The trend closely follows the HVAC energy savings, with greater reductions in warmer regions due to the enhanced radiative cooling performance. Additionally, the dynamic electrochromism further reduces CO_2 emissions associated with electricity consumption, as most cooling demand is met by electricity, whereas heating primarily relies on natural gas. On average, this electrochromic device can help U.S. buildings reduce CO_2 emissions by approximately 4063 kgCO_2 per year.

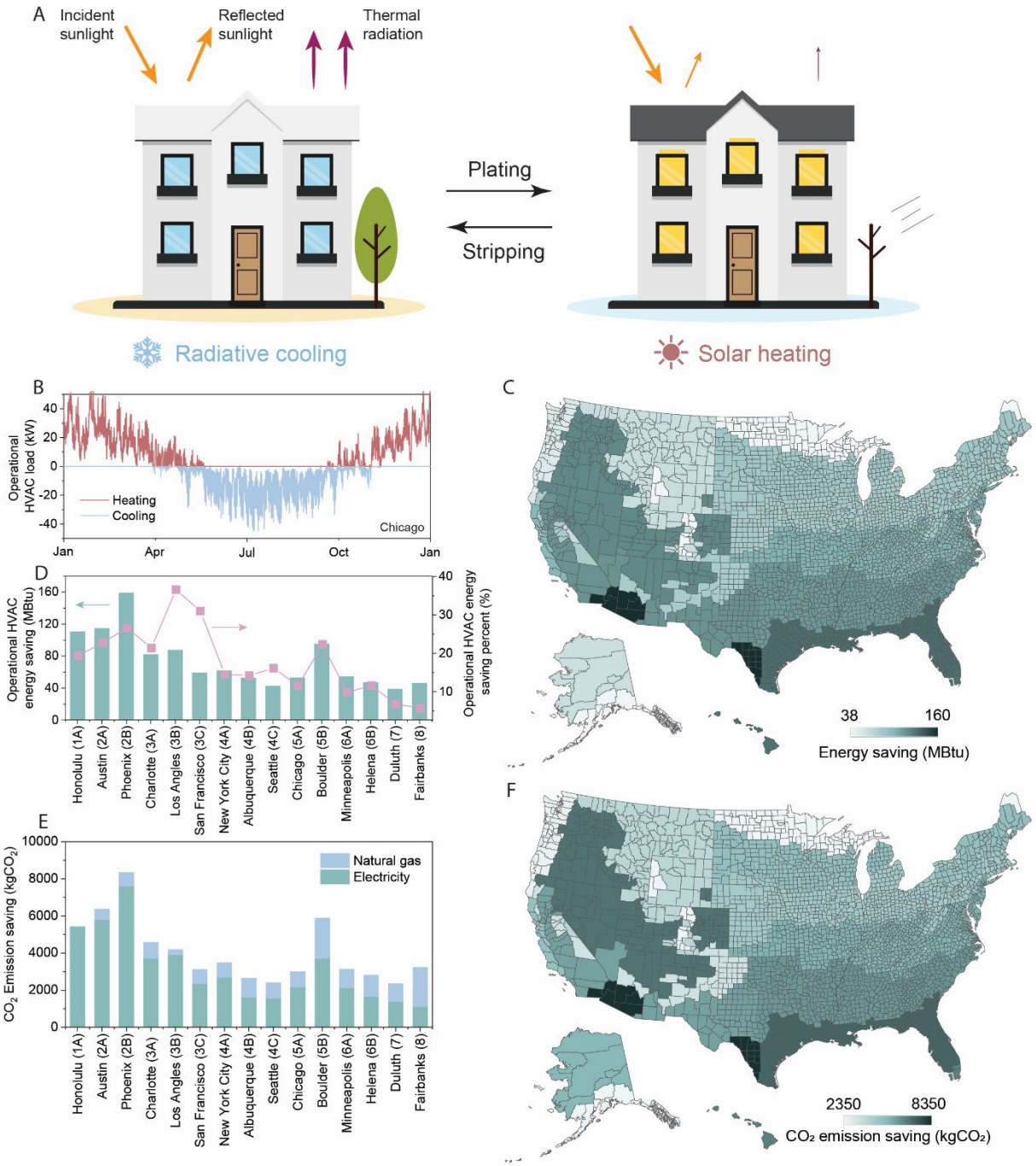

Figure 6. Energy Saving Capability (A) Illustration of energy-efficient buildings equipped with the developed electrochromic device, demonstrating its dual-mode functionality for heating and cooling. (B) Annual operational HVAC loads for a mid-rise apartment in Chicago. (C) U.S. energy-saving map highlighting the regional effectiveness of the device in reducing HVAC energy consumption. (D) Operational HVAC energy savings and corresponding percentage reductions achieved in

selected U.S. cities. (E) Annual CO_2 emission saving in selected U.S. cities. (F) U.S. annual CO_2 emission saving map.

Discussion

In this study, we successfully developed an electrochromic device capable of dynamically regulating solar radiation and thermal emissivity, providing a promising solution for reducing energy consumption in buildings. The device combines the synergistic tuning of solar and mid-infrared optical properties, achieving efficient solar heating during cold weather and sub-ambient radiative cooling during hot weather. By leveraging Cu-Bi amorphous nanoparticles and optimizing the electrochemical deposition process, we demonstrated the feasibility of this device for year-round energy savings. The integration of the electrochromic device into building envelopes holds significant potential for reducing HVAC loads and operational energy consumption, especially in regions with hot climates.

The *EnergyPlus* simulations revealed that the electrochromic device could save an average of 73.69 MBtu annually across different regions in the U.S., with more pronounced savings in warmer climates due to its effective radiative cooling capabilities. This suggests that, while the device performs well across various geographic locations, future efforts should focus on enhancing solar heating efficiency, particularly in cooler regions. Challenges remain in optimizing solar heating performance and achieving greater efficiency in colder climates. Nevertheless, the situation may be subject to change given the rising global temperature. While the device's ability to switch between heating and cooling modes based on external conditions offers great promise, further improvements in material selection, electrochemical processes, and device architecture are necessary to fully realize its potential. Additionally, scaling the technology for widespread commercial application will require further research into cost-effectiveness, durability, and long-term performance under real-world conditions.

In conclusion, the electrochromic adaptive solar heater and radiative cooler presented in this work provide a novel and effective approach to building energy management. Its versatility in tuning optical properties in response to ambient conditions offers a sustainable, low-energy solution for enhancing building energy efficiency. Continued optimization and research are crucial for addressing the challenges posed by seasonal climate variations and unlocking the full potential of this technology for widespread adoption in energy-efficient buildings. Moreover, its non-destructive retrofitting capability presents an exciting opportunity for enhancing energy performance in existing infrastructure, making it a compelling option for the global energy transition.

Method

Electrolyte preparation

The aqueous electrolyte consists of 10 mM $Cu(ClO_4)_2$, 10 mM $BiOClO_4$, 1 M $LiClO_4$, 10 mM $HClO_4$ and 10% (wt.) poly(vinyl alcohol) for uniform electrodeposition. The whole solution was mixed under 80 °C.

Electrochromic building envelope fabrication

The monolayer graphene is purchased from CheapTube Inc., which is CVD-grown on Cu foil. The Cu-graphene sample is hot-pressed onto 20 μm PE film at 99 °C, and then the Cu is dissolved in 1M $FeCl_3$ solution. Finally, the sandwiched sample is rinsed with DI water to form a transparent conductive electrode.

The copper tape is used as a counter electrode and is taped on the silver mylar. The Kapton tape with 20 μm thickness is used as the separator. Then the transparent electrode is attached to the top to seal the electrode in between.

Cross-sectional TEM characterization

After deposition, the film was embedded into Poly/Bed 812 resin to get cross-section view images and cut into 90-nm-thick slides using an ultramicrotome (Ultracut E, Reichert-Jung). High-angle annular dark-field (HAADF) imaging and selected area electron diffraction (SAED) were conducted with the aberration-corrected scanning transmission electron microscope JEOL ARM200CF (200 kV) at the University of Illinois at Chicago. EDS spectrum imaging was performed using an Oxford X-Max 100TLE windowless SDD detector.

Outdoor temperature testing

The device was first electrically biased prior to testing to achieve its optimal cooling and heating states. Owing to its non-volatile nature, the device retained its optical properties throughout the entire testing period. It was then mounted onto a copper plate, which was attached to a vacuum insulation panel to minimize parasitic heat losses. The insulation panel was wrapped in Ag-coated Mylar for enhanced thermal isolation. Finally, the top surface of the device was covered with 80 μm PE film to partially block solar radiation, thereby enhancing radiative cooling performance and reducing convective heat loss.

Building energy saving calculation

We employed *EnergyPlus*, an open-source whole-building energy simulation tool (https://energyplus.net/), to estimate HVAC energy consumption throughout the year. *EnergyPlus* simulates realistic buildings using a heat balance-based approach to account for all heat transfer processes on both internal and external surfaces. The

software incorporates various loads, including equipment, occupants, and lighting, while ensuring occupants' thermal comfort. It solves the energy balance equation hourly over the entire year, considering the interaction between indoor (room temperature) and outdoor (ambient temperature based on weather data) conditions.

HVAC energy consumption was modeled across different U.S. regions using *EnergyPlus* version 9.4. Fifteen cities were selected to represent the diverse climate zones in the United States. The simulations used hourly weather data from a typical meteorological year (TMY2). The model utilized was the "new-2004 midrise apartment" from the U.S. Department of Energy. This building had a rectangular design with a total floor area of 783.75 m² (length: 46.33 m, width: 16.91 m, height: 12.19 m), four stories, and a window-to-wall ratio of 15%. Baseline simulations were conducted with standard wall properties (default settings as downloaded). Cooling and heating loads were calculated on an hourly basis for the entire year.

CO_2 emission saving calculation

We calculated the daily CO_2 emission factor of electricity generation in the US for the latest available year, 2024. The approach follows IPCC (2006) guidelines to ensure consistency and accuracy. (*49*)

The calculation of CO_2 emission factors relies on multiple datasets:

- Electricity generation data by energy source: Obtained from the U.S. Energy Information Administration's (EIA) Hourly Electric Grid Monitor (https://www.eia.gov/beta/electricity/gridmonitor/), covering various energy sources.
- Emission factors by energy source: Extracted from the U.S. EIA State Electricity Profiles (https://www.eia.gov/electricity/state/unitedstates/state_tables.php), measured in pounds per kilowatt-hour (pounds/kWh).

The study includes the following primary energy sources: 1) Coal, 2) Natural Gas, 3) Petroleum, and 4) All Other Energy Sources (including fossil fuels, specific geothermal power plants, and other sources)

Electricity generation from hydro, solar, and wind is treated as carbon neutral, in accordance with EIA guidelines.

The CO_2 emission factor is calculated as follows:

$$EF = \frac{\sum(AD_k \times EF_k)}{\sum AD_k}$$

Where k reflects the energy sources considered in the calculation. In our study, k covers three primary fossil fuels types which are Coal, Petroleum, Natural-gas along

with a category labeled All Other Energy Sources. AD_k represents the activity data, which refers to the amount of electricity generated by each energy source k. The electricity generation data for various energy sources is obtained from the U.S. Energy Information Administration's (EIA) Hourly Electric Grid Monitor. EF_k represents the emission factor, defined as the amount of CO_2 emissions produced per unit of electricity generation for energy source k. The emission factors for various energy sources are collected from U.S. EIA State Electricity Profiles, as shown in Supplementary Table 1. Finally, Supplementary Fig. 10 presents the estimated daily CO_2 emission factor of electricity generation in the U.S. for 2024, measured in kg CO_2 per kWh. The emission factor of natural gas for homes is collected from the U.S. Energy Information Administration's (EIA) Carbon Dioxide Emissions Coefficients by Fuel (https://www.eia.gov/environment/emissions/co2_vol_mass.php). The CO_2 factor of natural gas for homes and businesses is 52.91 Kilograms CO_2 Per Million Btu.

Contributions

P.-C.H. and C.S. conceived the idea. C.S. performed all the experiments, building energy simulation, and corresponding data analyses. Q.L. did the COMSOL optical simulation. Y.H. conducted the cross-sectional TEM and EDX mapping. X.D. and C.S. did the CO_2 emission calculation. C.S., J.P. and P.-C.H. wrote the manuscript with input from all co-authors.

Acknowledgements

We thank C. Liu (University of Chicago, Pritzker School of Molecular Engineering) for the valuable discussion regarding pulse electrodeposition, G. Tan (Zhejiang University) for kindly helping with the building energy saving calculation. The project was partially sponsored by the Collaboration Grants for Climate Change from Nicholas Institute for Energy, Environment & Sustainability and the startup fund by Pratt School of Engineering at Duke University and Pritzker School of Molecular Engineering at the University of Chicago. P.-C. H. acknowledges support from the National Science Foundation under award number NSF ECCS-2324286.

Data availability

All data needed to support the conclusions in the paper are present in the manuscript and/or Supplementary Information. Additional data related to this paper may be requested from the corresponding authors.

Competing interests

P.-C.H. and C.S. have a 2021 US patent application (63/256,136). The other authors declare no competing interests.

References

1. *Heating and Cooling*.
2. D. M. Kammen, D. A. Sunter, City-integrated renewable energy for urban sustainability. *Science* **352**, 922-928 (2016).
3. T. Li *et al.*, A radiative cooling structural material. *Science* **364**, 760-763 (2019).
4. L. Zhao, X. Lee, R. B. Smith, K. Oleson, Strong contributions of local background climate to urban heat islands. *Nature* **511**, 216-219 (2014).
5. F. Cao, K. McEnaney, G. Chen, Z. Ren, A review of cermet-based spectrally selective solar absorbers. *Energy & Environmental Science* **7**, 1615-1627 (2014).
6. T. S. Eriksson, C. G. Granqvist, Radiative cooling computed for model atmospheres. *Appl. Opt.* **21**, 4381-4388 (1982).
7. D. Kraemer *et al.*, High-performance flat-panel solar thermoelectric generators with high thermal concentration. *Nature Materials* **10**, 532-538 (2011).
8. X. Li *et al.*, Graphene oxide-based efficient and scalable solar desalination under one sun with a confined 2D water path. *Proceedings of the National Academy of Sciences* **113**, 13953-13958 (2016).
9. J. Mandal *et al.*, Scalable, "Dip-and-Dry" Fabrication of a Wide-Angle Plasmonic Selective Absorber for High-Efficiency Solar–Thermal Energy Conversion. *Advanced Materials* **29**, 1702156 (2017).
10. A. P. Raman, M. A. Anoma, L. Zhu, E. Rephaeli, S. Fan, Passive radiative cooling below ambient air temperature under direct sunlight. *Nature* **515**, 540-544 (2014).
11. N. N. Shi *et al.*, Keeping cool: Enhanced optical reflection and radiative heat dissipation in Saharan silver ants. *Science* **349**, 298-301 (2015).
12. R. Wu *et al.*, Spectrally engineered textile for radiative cooling against urban heat islands. *Science* **384**, 1203-1212 (2024).
13. S. Zeng *et al.*, Hierarchical-morphology metafabric for scalable passive daytime radiative cooling. *Science* **373**, 692-696 (2021).
14. Y. Zhai *et al.*, Scalable-manufactured randomized glass-polymer hybrid metamaterial for daytime radiative cooling. *Science* **355**, 1062-1066 (2017).
15. L. Zhou *et al.*, A polydimethylsiloxane-coated metal structure for all-day radiative cooling. *Nature Sustainability* **2**, 718-724 (2019).
16. X. Li *et al.*, Integration of daytime radiative cooling and solar heating for year-round energy saving in buildings. *Nature Communications* **11**, 6101 (2020).
17. X. Li, W. Xie, C. Sui, P.-C. Hsu, Multispectral Thermal Management Designs for Net-Zero Energy Buildings. *ACS Materials Letters* **2**, 1624-1643 (2020).
18. I. Sartori, A. Napolitano, K. Voss, Net zero energy buildings: A consistent definition framework. *Energy and Buildings* **48**, 220-232 (2012).
19. R. Baetens, B. P. Jelle, A. Gustavsen, Properties, requirements and possibilities of smart windows for dynamic daylight and solar energy control in buildings: A state-of-the-art review. *Solar Energy Materials and Solar Cells* **94**, 87-105 (2010).
20. Y. Rao *et al.*, Ultra-Wideband Transparent Conductive Electrode for Electrochromic Synergistic Solar and Radiative Heat Management. *ACS Energy Letters* **6**, 3906-3915 (2021).
21. W. Cheng *et al.*, Photodeposited Amorphous Oxide Films for Electrochromic Windows. *Chem* **4**, 821-832 (2018).

22. N. L. Sbar, L. Podbelski, H. M. Yang, B. Pease, Electrochromic dynamic windows for office buildings. *International Journal of Sustainable Built Environment* **1**, 125-139 (2012).
23. S. Lin *et al.*, A Flexible, Robust, and Gel-Free Electroencephalogram Electrode for Noninvasive Brain-Computer Interfaces. *Nano Letters* **19**, 6853-6861 (2019).
24. N. Liu *et al.*, Ultratransparent and stretchable graphene electrodes. *Science Advances* **3**, e1700159.
25. S. Seo, M. Min, S. M. Lee, H. Lee, Photo-switchable molecular monolayer anchored between highly transparent and flexible graphene electrodes. *Nature Communications* **4**, 1920 (2013).
26. H. Wu *et al.*, A transparent electrode based on a metal nanotrough network. *Nature Nanotechnology* **8**, 421-425 (2013).
27. A. Llordés, G. Garcia, J. Gazquez, D. J. Milliron, Tunable near-infrared and visible-light transmittance in nanocrystal-in-glass composites. *Nature* **500**, 323-326 (2013).
28. M. T. Strand *et al.*, Polymer inhibitors enable >900 cm2 dynamic windows based on reversible metal electrodeposition with high solar modulation. *Nature Energy* **6**, 546-554 (2021).
29. C. Yan *et al.*, Stretchable and Wearable Electrochromic Devices. *ACS Nano* **8**, 316-322 (2014).
30. M. S. Ergoktas *et al.*, Multispectral graphene-based electro-optical surfaces with reversible tunability from visible to microwave wavelengths. *Nature Photonics* **15**, 493-498 (2021).
31. M. Li, D. Liu, H. Cheng, L. Peng, M. Zu, Manipulating metals for adaptive thermal camouflage. *Science Advances* **6**, eaba3494.
32. J. Mandal *et al.*, Li4Ti5O12: A Visible-to-Infrared Broadband Electrochromic Material for Optical and Thermal Management. *Advanced Functional Materials* **28**, 1802180 (2018).
33. O. Salihoglu *et al.*, Graphene-Based Adaptive Thermal Camouflage. *Nano Letters* **18**, 4541-4548 (2018).
34. C. Geng *et al.*, Adaptive Variable Emissivity Reflector for Seasonal and Daily Thermal Regulation in Regions with Significant Temperature Variations. *Advanced Functional Materials* **34**, 2410819 (2024).
35. C. Sui, P.-C. Hsu, Standardizing the Thermodynamic Definition of Daytime Subambient Radiative Cooling. *ACS Energy Letters* **9**, 2997-3000 (2024).
36. K. S. Kim *et al.*, Large-scale pattern growth of graphene films for stretchable transparent electrodes. *Nature* **457**, 706-710 (2009).
37. L. Fuller, J. Martin, Y. Ma, S. King, S. Sen, Control of Texture and Morphology of Zinc Films through Pulsed Methods from Additive-Free Electrolytes. *ChemistrySelect* **6**, 5426-5434 (2021).
38. G. Garcia, E. Ventosa, W. Schuhmann, Complete Prevention of Dendrite Formation in Zn Metal Anodes by Means of Pulsed Charging Protocols. *ACS Applied Materials & Interfaces* **9**, 18691-18698 (2017).
39. N. Ibl, J. C. Puippe, H. Angerer, Electrocrystallization in pulse electrolysis. *Surface Technology* **6**, 287-300 (1978).

40. C. Sui *et al.*, Dynamic electrochromism for all-season radiative thermoregulation. *Nature Sustainability* **6**, 428-437 (2023).
41. A. Schlegel, P. Wachter, K. P. Ackermann, M. Liard, H. J. Güntherodt, Optical properties of metallic glasses. *Solid State Communications* **31**, 373-376 (1979).
42. O. Teppo, J. Niemelä, P. Taskinen, An assessment of the thermodynamic properties and phase diagram of the system Bi-Cu. *Thermochimica Acta* **173**, 137-150 (1990).
43. M. Caplan, J. Trouba, C. Anderson, S. Wang, Hydrometallurgical Leaching of Copper Flash Furnace Electrostatic Precipitator Dust for the Separation of Copper from Bismuth and Arsenic. *Metals* **11**, 371 (2021).
44. C. She *et al.*, Robust long-term stable reversible Bi-Cu alloy electrodeposition across 100 °C temperature range. *Chemical Engineering Journal* **509**, 161290 (2025).
45. Y. Yamada *et al.*, Hydrate-melt electrolytes for high-energy-density aqueous batteries. *Nature Energy* **1**, 16129 (2016).
46. D. C. Madu, A. A. Thompson, M. J. Leahy, M. V. Lilo, C. J. Barile, Water-in-Salt Electrolytes for Reversible Zinc Electrodeposition for Dynamic Windows. *Journal of The Electrochemical Society* **170**, 112502 (2023).
47. J. Liang *et al.*, Ionic Liquid-Based Reversible Metal Electrodeposition for Adaptive Radiative Thermoregulation Under Extreme Environments. *Advanced Functional Materials* **n/a**, 2419087 (2025).
48. J. Y. Li *et al.*, Bi-Cu Electrolytes with Aminocarboxylate Chelators for Reversible Metal Electrodeposition at High pH for Dynamic Windows. *Journal of The Electrochemical Society* **170**, 062505 (2023).
49. IPCC (2006). 2006 IPCC Guidelines for National Greenhouse Gas Inventories. https://www.ipcc-nggip.iges.or.jp/public/2006gl/.